Die approbierte Originalversion dieser Diplom-/Masterarbeit ist in der Hauptbibliothek der Technischen Universität Wien aufgestellt und zugänglich.
http://www.ub.tuwien.ac.at

The approved original version of this diploma or master thesis is available at the main library of the Vienna University of Technology.
http://www.ub.tuwien.ac.at/eng

Masterthesis

Numerical investigation of the flow in a cylinder with a rotating lid

ausgeführt zum Zwecke der Erlangung des akademischen Grades des
Master of Science in Engineering (MSc)
unter der Leitung von

Univ.Ass. Francesco Romanò, PhD.
und
Univ.Prof. Dipl.-Phys. Dr.rer.nat. Hendrik C. Kuhlmann
Institutsnummer E322
Institut für Strömungsmechanik und Wärmeübertragung

eingereicht an der Technischen Universität Wien

Fakultät für Verfahrenstechnik

von

Michael Riedl, BSc
Matrikelnummer 1429308
Webergasse 25/20, 1200 Wien

Wien, 18 Mai 2018

Abstract

The concerned motion of fluid within a cylindrical tank driven by the axisymmetrical rotation of the top lid is a well established benchmark problem for computational fluid dynamics. Yet, regardless of the simplicity of its geometry, it exhibits a variety of remarkable fluid dynamical phenomena.

Applying the spectral element solver Nek5000, we simulate fluid dynamical structures reported in literature. An agreement of computational results with experimental measurements has been shown for vortex breakdowns, the onset of which we determine for a variety of Reynolds numbers and aspect ratios. For mentioned range we furthermore show the onset of traveling waves. We compute the streamlines in combination with Poincarè sections to study the flow even further by determining the sensitivity of these structures to artificial constructed perturbations.

Results suggest that the primary swirling motion of the flow dominates rendering the streamlines of the flow regular even when ideal or perturbed travelling waves occur. Also the system exhibits a complex streamline topology, wherein two saddle foci are connected via a degenerate heteroclinic connection.

Acknowledgements

Even though the authors name shown is mine, the complete list of names belonging to people who contributed in various ways to the completion of this thesis remains hidden at the cover page. Therefore and in an attempt to show my gratitude, I want to point out a handful of people, who were significantly involved in me writing and successfully finishing this thesis. Starting with those who have taught me the set of abilities to get me to this point in my life.

My father, who showed me the fascination and value within knowledge and broadened my perspective. My mother, who was an unbendable pillar of emotional support. My sister, who challenged me in a natural manner for siblings all my life to raise my tolerance level sufficiently high to survive the study of engineering.

Furthermore, I want to thank those who supported me during the past years. First of all I want to thank Astrid, who kept my body nourished and supported my mental hygiene. Who patiently listened to my confused monologues during long walks, when I desperately tried to get things straight in my head. Thank you for being the supportive partner that you are and thank you for the honor of your love.

Secondly I want to thank Belinda for being the best mother one could imagine for this wonderful child you gifted me. All this would not have been possible without your and your mothers support over all these years since we first met. I also want to thank your husband Florian, who treats Aurora as his own and who has been the partner you deserved and I could not have been.

Conclusively I want to thank those who supervised me. Professor Hendrik Kuhlmann, for giving me the opportunity to see the difference between hydraulics and fluid-dynamics, for giving me the time I needed to finish this thesis and any further support in pursuing my career.

Francesco, who guided me along this path, who supported me like no second person ever could. For being the perturbation that changed the trajectory of my life and lured me into science, for which I am really grateful. Thank you for showing me how true dedication in the search for answers and knowledge looks like and for all those hours we spend together. May the Romanò number soon be introduced.

While I am writing these last lines of this thesis, I want to thank all of you mentioned here and

those who are not mentioned but who kept me going through the past years and without their support this would not have been able to be accomplished.

Thank you all.

Dedication

To my daughter Aurora, who has been an inexhaustible source of motivation.

Most problems and their solutions are just separated by a simple na-na-na, practically...

Contents

Abstract **i**

Acknowledgements **iii**

1 Introduction **1**

1.1 Motivation and Objectives 1

2 Problem Description **3**

2.1 Geometry 3

2.2 Driving Force 4

2.3 Boundary Conditions 4

2.4 Dynamic Equations 5

3 Methodology **8**

3.1 General 8

3.2 Spectral Element Method 9

3.2.1 Spatial discretization 10

3.2.2 Temporal discretization 13

3.2.3 Applied Grids 15

3.3 Streamline 16

4 Results **18**

4.1 Flow 18

4.2 Vortex Breakdown 19

4.3 Traveling Waves 24

4.4 Streamline Topology 28

4.4.1 Perturbed Flow 30

5 Conclusion **33**

Bibliography **35**

Chapter 1

Introduction

1.1 Motivation and Objectives

Independent of their driving forces, either temperature gradients or moving boundaries, cavity models in fluid dynamics are of significant scientific interest [1]. In particular cylindrical enclosures with a moving boundary can be found in many engineering applications such as fixed-geometry swirl generators, which are typically applied in combustors of large industrial gas turbines for electric-power generation [2]. The residence time in the primary combustion chamber can be extended by creating a localized recirculation zone. Due to the increased turbulence intensity inside this zone, mixing of fuel and air is increased. This leads to a stable, compact flame. Furthermore, one can find similar setups in chemical reactors, mixing tanks and boilers [3]. These application designs include obstacles to disperse and stirrers to drive the fluid, which can be considered to be challenging from a numerical point of view. However, a simplified lid-driven cylindrical container system can provide useful insights in the dynamics of mentioned applications.

The behavior of the steady-swirling flow produced in a cylindrical experiment was already investigated in 1968 [4]. The inward spiraling fluid motion was visualized and revealed the occurrence of a recirculation bubble on the axis of symmetry, which is interpreted as a vortex breakdown. A systematical investigation showed that for certain conditions up to three vor-

tex breakdowns can simultaneously occur [5]. Furthermore, non-axisymmetric instabilities, so called traveling waves, were numerically discovered [6] and experimentally shown [7].

The lid-driven cylindrical tank has been investigated intensively over the past decades, systematically identifying a variety of occurring phenomena [4–7]. This thesis is concerned with following up the existing work and contributing further to an in-depth understanding using the spectral element solver NEK5000 to perform numerical simulations with high accuracy. Initially validating results of the axisymmetric vortex-breakdown with measurement data of Escudier [2], and further results of the non-axisymmetric instability with simulations by Gelfgat et. al [6]; subsequently computing streamlines in a range of different angular velocities to determine whether or not localized chaos occurs within the swirling motion.

Chapter 2

Problem Description

This chapter is concerned with the problem setup, which is treated numerically within the frame of this thesis. By describing separately the geometry, the driving force, boundary conditions and governing equations we want to emphasize key aspects of the computational challenges arising and approaches to their solution.

2.1 Geometry

The geometry of interest is a circular upright cylinder, which is general defined by its height H and radius R. By taking the ratio of height to radius one can reduce the geometric parameter

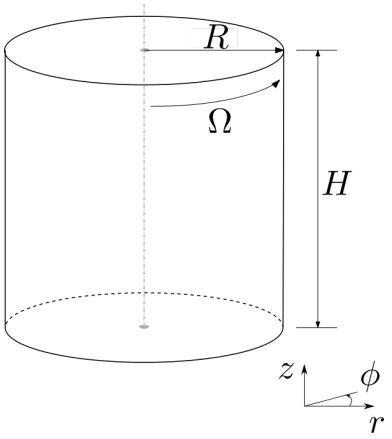

Figure 2.1: Sketch of the geometry. Showing the parameters height H, radius R and angular velocity Ω.

space to a single parameter, which is referred to as the aspect ratio, which is defined by equation 2.1.

$$\gamma = \frac{H}{R} \tag{2.1}$$

2.2 Driving Force

The system is driven by the angular velocity Ω of the top lid. Similar to the experimental setup of the unconfined rotating disc by von Kármán [8] the rotating endwall acts as a pump, driving the setup by drawing in fluid axially and ejecting it in an outward directed spiral.

The only dimensionless control parameter for the fluid motion is the Reynolds number, commonly defined as $Re = u\ d/\nu$ First introduced by O. Reynolds [9] for pipe flow. Wherein u was defined being the bulk velocity, d the inner pipe diameter and ν the kinematic viscosity. Generalizing, one can think of it as the ratio of inertial forces to viscous forces within a fluid. Adapting Re to the lid driven cylinder system by defining $u = \Omega\ R$ and $d = R$ results in equation 2.2.

$$Re = \frac{\Omega\ R^2}{\nu} \tag{2.2}$$

2.3 Boundary Conditions

Considering the boundaries being walls, which are impermeable to mass, leads to the constraint that the velocity normal component to that surface is zero. With $\mathbf{n}$ denoting the normal to the surface and $\boldsymbol{u}$ being the velocity vector, this can be expressed as

$$\boldsymbol{u} \cdot \boldsymbol{n} = 0 \tag{2.3}$$

Whereas the tangential components of the fluid can be considered as

$$\boldsymbol{u} - \boldsymbol{n}(\boldsymbol{n} \cdot \boldsymbol{u}) = \boldsymbol{\Psi} \tag{2.4}$$

Equation 2.4 describes the velocity of the fluid and the velocity of the wall Ψ, which is assumed to be zero in case of a stationary wall and $\boldsymbol{\Psi} = \Omega r \boldsymbol{e}_\varphi$ in case of the moving top lid, where r is the radial coordinate, Ω is angular velocity and $\boldsymbol{e}_\varphi$ is the unit vector in azimuthal direction. This assumption results in the no-slip boundary conditions for all walls. Both conditions lead to a singularity along the circumference of the rotating lid, where no-slip and moving-wall boundary conditions are simultaneously enforced. To resolve this singularity we included a monomial filtering approach. Based on an asymptotic assumption, the flow field is expanded at the elements which touch the singular border using a coordinate which accounts for the distance from the singular edge. The monomial filtering takes into account a monomial expansion in terms of distance from the edge of this intersection between the steady and the rotating wall based on this coordinate.

2.4 Dynamic Equations

The governing equations, which describe the dynamical motion of viscous fluids were derived in 1822 by two mathematicians, Claude-Louis Navier and George Gabriel Stokes, which they were named after. The Navier-Stokes equations are strictly a statement of the balance of momentum. These partial differential equations can basically be derived from applying the laws of motion to a fluid volume element. However, by using momentum instead of forces, which allows to calculate with conservation approaches rather than force balances lead, for a Newtonian fluid of constant viscosity μ and density ρ to the general form of:

$$\frac{\partial \boldsymbol{u}}{\partial t} + (\boldsymbol{u} \cdot \nabla)\boldsymbol{u} = -\frac{1}{\rho}\nabla p + \nu \nabla^2 \boldsymbol{u} + \boldsymbol{g} \tag{2.5}$$

When looking at equation 2.5, it is important to be aware of the interpretation of the individual terms.

$$\overbrace{\underbrace{\frac{\partial \boldsymbol{u}}{\partial t}}_{\text{variation}} + \underbrace{(\boldsymbol{u} \cdot \nabla)\boldsymbol{u}}_{\text{convection}}}^{\text{inertial force}} = \overbrace{\underbrace{-\frac{1}{\rho}\nabla p}_{\text{pressure}} + \underbrace{\nu \nabla^2 \boldsymbol{u}}_{\text{viscous forces}}}^{\text{divergence of stress}} + \underbrace{\boldsymbol{g}}_{\text{external forcing}}$$

The first term $\frac{\partial \boldsymbol{u}}{\partial t}$ describes the temporal variation in the flow velocity, e.g. the flow which develops starting from rest after the lid impulsively stats to rotate. The second term $(\boldsymbol{u} \cdot \nabla)\boldsymbol{u}$ is in the form of an advection term, i.e. $(\boldsymbol{u} \cdot \nabla)A$, which describes the transport of a quantity A due to the velocity $\boldsymbol{u}$, whereas in our case A is represented by the three components of the vector $\boldsymbol{u}$ for the three momenta. Such a transport occurs every time the quantity A is a non-uniform field, which admits a gradient, and the transport velocity $\boldsymbol{u}$ is non-parallel to the gradient, which is a typical case in cavity flows like the one we consider. On the right hand side of 2.5 the external forcing term $\boldsymbol{g}$ describes an acceleration term. The term $-\frac{1}{\rho}\nabla p$ shows influences resulting of a pressure gradient on the flow field, e.g. a pressure force to drive the system. Whereas ϱ describes the density of the fluid. The remaining term $\nu \nabla^2 \boldsymbol{u}$ represents viscous forces due to friction.

Introducing a reference velocity U and a reference length L equation 2.5 can be non-dimensionalized by introducing following non-dimensional variables $\hat{\boldsymbol{x}} = \boldsymbol{x}/L$ for space, $\hat{\boldsymbol{u}} = \boldsymbol{u}/U$ for velocity, $\hat{t} = t/(L/U)$ for time, $\hat{p} = p/(\rho U^2)$ for pressure for flows dominated by convective effects and $\hat{\boldsymbol{g}} = \boldsymbol{g}L/(U^2)$ for external acceleration, leading to the non-dimensionalized form:

$$\frac{\partial \hat{\boldsymbol{u}}}{\partial \hat{t}} + (\hat{\boldsymbol{u}} \cdot \nabla)\hat{\boldsymbol{u}} \ = -\nabla \hat{p} + \frac{1}{Re}\nabla^2 \hat{\boldsymbol{u}} + \hat{g} \tag{2.6}$$

To further fully describe the flow of a fluid, more information is needed, how much depends on the assumptions made. Next to the information already treated like boundary conditions and now balance of momentum, also the conservation of mass has to be formulated. In a general form one can formulate this as in equation 2.7.

$$\frac{\partial \rho}{\partial t} + \nabla \cdot (\rho \boldsymbol{u}) = 0 \tag{2.7}$$

Which is in called continuity equation. By furthermore assuming, as we did for eq. 2.5, the

fluid dealt with to be incompressible, one can rewrite equation 2.7 as:

$$\nabla \cdot \boldsymbol{u} = 0 \tag{2.8}$$

The properties of the Navier-Stokes equations, being non-linear partial differential equations, result in a complex approach to find analytical solutions in simple geometries. However, a general solution still has to be derived, if existent. This circumstance contributes on one hand to the scientific interest in fluid dynamical problems, on the other hand to the complexity of flows even in rather simple geometries. The flow in a cylinder can be considered as a geometrically simple setup, whereas the motion of the fluid within it is anything but trivial.

Chapter 3

Methodology

3.1 General

For solving a given numerical problem one faces the act of balancing accuracy and computational costs by choosing the applied numerical method. Simply increasing the overall accuracy leads to a significant increase in computational cost. Therefore, it is desirable to obtain the possibility of limiting the increase of accuracy in certain areas of interest. Finite element methods provide such a possibility by locally refining the computational grids, but lack on the overall accuracy of spectral methods, provided through their spectral properties. A combination of both methods seems desirable, which was introduced by A. Patera in 1984 called spectral element method (SEM) [10]. Furthermore, this method was implemented in the incompressible fluid flow solver NEKTON by Paul Fischer, Lee Ho and Einar Rønquist, with technical input from A. Patera and Y. Maday. Paul Fischer developed a research version of the original code now known as Nek5000 [11], which we apply in the frame of this thesis. The code is written in Fortran 77 and C and provides an option for parallelization of processes via MPI. Nek5000 was recognized with Gordon Bell prize for algorithmic quality and sustained parallel performance.

3.2 Spectral Element Method

The key feature of the spectral element method (SEM) is the combination of the accuracy of Fourier spectral methods and the flexibility of methods based on low-order local approaches. SEM is using the high order weighted residual technique based on orthogonal polynomials and accurate numerical quadrature. Discretization nodes are defined using Gauss-Legendre-Lobatto (GLL) polynomials, which will be explained in more detail in section 3.2.1. In addition the method exhibits favorable computational properties, including tensor products and naturally diagonal mass matrices, good scalability and the possibility of using message passing interface (MPI) for parallel computing.

In the following sections, we will give an outline of the main steps of how the discretization can be accomplished. We apply it to an example of the one-dimensional, non-linear Burgers equation, we will follow the notation by Deville et al. [12] and Loiseau [13] . The Burgers equation serves frequently as a benchmark problem for Navier-Stokes equations since it exhibits properties such as non-linearity and important for modeling the turbulence.

$$\begin{cases} \partial u_t + u\partial u_x = v\partial_x^2 u \\ u(t=0,x) = u^0 \\ u(t,x=-1) = 1; u(t,x=1) = -1 \end{cases} \tag{3.1}$$

Wherein u denotes the velocity and ν the viscous coefficient and the computational domain considered is defined as $\Omega := \{x \in [-1,1]\}$. The key concepts for the discretization based on the Galerkin method are the so called "weak form" and the "Galerkin projection" in combination with "high-order basis functions". Therefore, let us focus on equation 3.1. One can recast it into its weak counterpart by using a set of test functions $v(x)$:

$$\int_\Omega v\frac{\partial u}{\partial t}dx + \int_\Omega vu\frac{\partial u}{\partial x}dx = -\nu\int_\Omega v\frac{\partial v}{\partial x}\frac{\partial u}{\partial x}dx \tag{3.2}$$

Here the right hand side of the equation has been treated using integration by parts. Now we

define $N+1$ basis functions ϕ_i.

$$\begin{cases} u(x,t) = \sum_{i=1}^{N} \phi_i(x) u_i(t) \\ v(x) = \phi_j \qquad 0 \leq j \leq N \end{cases} \tag{3.3}$$

inserting into the weak formulation of the Burgers equation leads to:

$$\left(\int_\Omega \phi_i \phi_j dx \right) \frac{du_i}{dt} + \left(\int_\Omega \phi_j \phi_i u_i \frac{d\phi_i}{dx} dx \right) u_i = - \left(\nu \int_\Omega \frac{d\phi_j}{dx} \frac{d\phi_i}{dx} dx \right) u_i \tag{3.4}$$

We define:

$$\begin{aligned} B_{i,j} &= \int_\Omega \phi_i \phi_j dx \\ C_{i,j}(\boldsymbol{u}_N) &= \int_\Omega \phi_j \phi_i \frac{d\phi_i}{dx} dx \\ K_{i,j} &= v \int_\Omega \frac{d\phi_j}{dx} \frac{\phi_i u}{dx} dx \end{aligned} \tag{3.5}$$

$B_{i,j}$ is considered as the mass matrix, $C_{i,j}(\boldsymbol{u}_N)$ is the convection operator applied on $\boldsymbol{u}_N = (u_0, ..., u_N)^T$ and $K_{i,j}$ is the stiffness matrix. Substituted into equation 3.4 leads to the matrix-vector form:

$$B \frac{d\boldsymbol{u}_N}{dt} + C(\boldsymbol{u}_N)\boldsymbol{u}_N + K\boldsymbol{u}_N = 0 \tag{3.6}$$

Numerical results for this system can be found in Deville et al. [12].

3.2.1 Spatial discretization

The internal meshing algorithm of Nek5000 uses Gauss-Legendre Lobatto formulae to spatially discretize the computation grid. Their main feature is, that the nodes are related to the stationary points of Legendre polynomials and include the extrema of the interval $(-1, 1)$. Additionally they are also represented by the maximum and minimum of the Legendre polynomial L_N of degree N. Therefore, the nodes $\{x_0 = -1, x_1, ..., x_{N-1}, x_N = 1\}$ are defined by the zeros

of the first derivative of the L_N with respect to x, which we denote by prime.

$$L'_N(x_i) = 0, \quad for \quad i = 1, ..., N-1. \tag{3.7}$$

For simplicity we forth on apply the notation by A. Quarteroni [14] for the following derivations. We define ψ_i to be the corresponding characteristic polynomials:

$$\psi_i \in \mathbb{Q}_{\mathbb{N}} : \quad \psi_i(x_i) = \delta_{ij}, \quad 0 \leq i, j \leq N, \tag{3.8}$$

which can be analytically formulated as:

$$\psi_i(x_i) = \frac{-1}{N(N+1)} \frac{(1-x^2)L'_N(x)}{(x-x_i)L_N(x_i)}, i = 0, ..., N \tag{3.9}$$

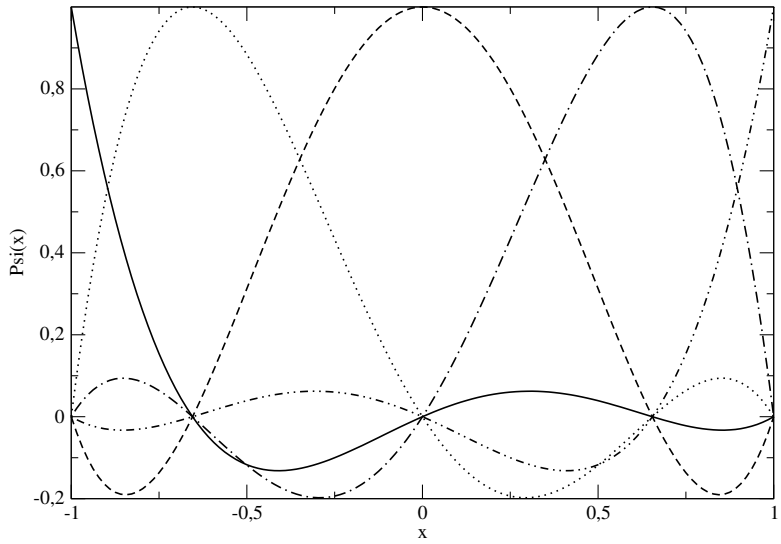

Figure 3.1: The characteristic polynomials ψ_i, for $i = 0, 1, 2, 3, 4$

Figure 3.2.1 shows the characteristic polynomials ψ_i for $N = 4$, wherein its maxima and minima give the location of the nodes.

The spectral elements approximation of $u_N^e(x)$ of degree N in the element Ω^e mapped onto the reference element $\hat{\Omega}$ is:

$$u_N^e(x) = \sum_{j=0}^{N} u_j^e \psi_i(x_i) \tag{3.10}$$

with $\{u_j^e\}_{j=0}^N$ the nodal values of the unknown scalar field u in Ω^e. Replacing $\phi(x)$ in equation 3.4 by equation 3.9 and applying Gaussian quadrature rule based on the GLL nodes to evaluate numerically the different integrals yields to:

$$\begin{aligned} B_{i,j}^e &= \frac{h_e}{2}\rho_i\delta_{ij} \\ C(\boldsymbol{u}_N)_{i,j} &= \rho_i u_i D_{N,ij}^1 \\ K_{i,j}^e &= \nu\frac{h_e}{2}\sum_{m=0}^{N}\rho_m D_{N,mi}^1 D_{N,mj}^1 \end{aligned} \tag{3.11}$$

Compared to equation 3.5, $B_{i,j}^e$ denotes the now discretised elementwise mass matrix, $C(\boldsymbol{u}_N)_{i,j}(\boldsymbol{u}_N)$ the non-linear convection operator and $K_{i,j}^e$ the discretised elementwise stiffness matrix. Further, we introduced ρ_i here as the GLL quadrature weight at the i^{th} GLL node. In addition we define D_N^1 such:

$$D_{N,ij}^1 = \frac{d\psi_i}{dx}(x=(x_i)) = \begin{cases} L_N(x_i)\left[L_N(x_j)(x_i-x_j)\right]^{-1}, & i\neq j, \\ -(N+1)N/4, & i=j=0, \\ (N+1)N/4, & i=j=N, \\ 0 \quad \text{otherwise} \end{cases} \tag{3.12}$$

The assembly of all elements Ω^e to the global matrices direct stiffness summation is applied. This operation is beyond the scope of this rapid introduction to spectral elements and the reader is referred to [12] or [14] for further information. Conclusively we read the semi-discretised equation as:

$$\boldsymbol{B}\frac{d}{dt}\boldsymbol{u}_N + \boldsymbol{C}(\boldsymbol{u}_N)\boldsymbol{u}_N + \boldsymbol{K}\boldsymbol{u}_N = 0 \tag{3.13}$$

The global stiffness matrix $\boldsymbol{K}$ and mass matrix $\boldsymbol{B}$ resulting from the direct stiffness summation. The mass matrix $\boldsymbol{B}$ exhibits a diagonal structure, whereas the stiffness matrix $\boldsymbol{K}$ exhibits a block diagonal structure.

3.2.2 Temporal discretization

Considering the established equation 3.13, this problem is formally equivalent to the semi-discretised formulation of the Navier-Stokes equation. The temporal discretisation scheme supported by Nek5000 are BDF/EXT and characteristics-based timestepping [15], both of which are accurate to the kth-order. However, while the viscous terms are treated implicitly via a kth order backward differentiation formula, the non-linear terms are discretised explicitly by an kth order extrapolation. For $k = 3$ we write the now fully discretised Burgers equation as:

$$\begin{aligned} \Big(\frac{11}{6\Delta t}\boldsymbol{M} + \boldsymbol{K}\Big)\boldsymbol{u}_N^{n+1} - \boldsymbol{D}_i^T\boldsymbol{p}^{n+1} = \\ = \frac{1}{\Delta t}\boldsymbol{M}\Big(3\boldsymbol{u}_N^n - \frac{3}{2}\boldsymbol{u}_N^{n-1} + \frac{1}{3}\boldsymbol{u}_N^{n-2}\Big) - \Big(3\boldsymbol{C}\boldsymbol{u}_N^n - 3\boldsymbol{C}\boldsymbol{u}_N^{n-1} + \boldsymbol{C}\boldsymbol{u}_N^{n-2}\Big) \end{aligned} \tag{3.14}$$

To recast equation 3.14 into a handy matrix form, we add $\boldsymbol{D}_i^T\boldsymbol{p}^n$ to both sides and rewriting the right-hand side as a forcing vector $\boldsymbol{M}\boldsymbol{F}_i^n$. Thus resulting in:

$$\begin{bmatrix} \boldsymbol{H} & -\boldsymbol{D}^T \\ -\boldsymbol{D} & 0 \end{bmatrix} = \begin{pmatrix} \boldsymbol{u}_N^{n+1} \\ \boldsymbol{\delta p}^{n+1} \end{pmatrix} \begin{pmatrix} \boldsymbol{M}\boldsymbol{F}^n + \boldsymbol{D}^T\boldsymbol{p}^n \\ 0 \end{pmatrix} \tag{3.15}$$

$\boldsymbol{H}$ being the Helmholtz operator. Furthermore, we introduce a matrix $\boldsymbol{Q}$ to project the original matrix onto a divergence-free space. Within a two-step treatment we remodel the system of equation into:

$$\begin{bmatrix} \boldsymbol{H} & 0 \\ -\boldsymbol{D} & -\boldsymbol{D}\boldsymbol{Q}\boldsymbol{D}^T \end{bmatrix} = \begin{pmatrix} \boldsymbol{u}_N^{*} \\ \boldsymbol{\delta p}^{n+1} \end{pmatrix} \begin{pmatrix} \boldsymbol{M}\boldsymbol{F}^n + \boldsymbol{D}^T\boldsymbol{p}^n \\ 0 \end{pmatrix} \tag{3.16}$$

and

$$\begin{bmatrix} \boldsymbol{I} & -\boldsymbol{Q}\boldsymbol{D}^T \\ -\boldsymbol{D} & \boldsymbol{I} \end{bmatrix} = \begin{pmatrix} \boldsymbol{u}_N^{*} \\ \boldsymbol{\delta p}^{n+1} \end{pmatrix} \begin{pmatrix} \boldsymbol{M}\boldsymbol{F}^n + \boldsymbol{D}^T\boldsymbol{p}^n \\ 0 \end{pmatrix} \tag{3.17}$$

Choosing the matrix $\boldsymbol{Q}$ defines the applied projection method. Nek5000 sets $\boldsymbol{Q}$ to:

$$\boldsymbol{Q} = \boldsymbol{H}^{-1} \tag{3.18}$$

leading to the Uzawa algorithm [16], which exact solution is for the inverse Helmoltz operator is computational intensive. Therefore, the Blair-Perot algorithm is implemented within Nek5000, changing the projection matrix to $\boldsymbol{Q} = \gamma \boldsymbol{M}^{-1}/\Delta t$ with $\gamma = 11\Delta t/6$. One can find further elaborations on temporal discretisation and projection methods applied in Nek5000 in [12].

3.2.3 Applied Grids

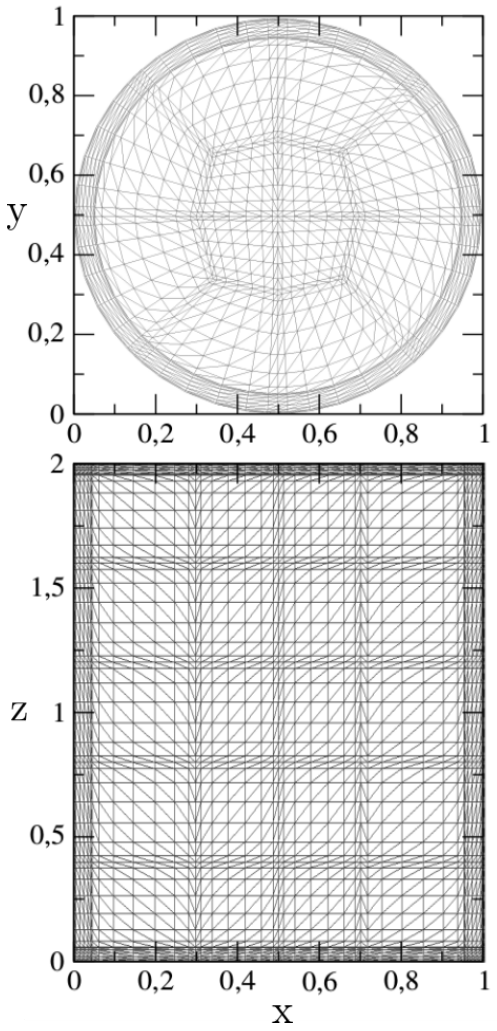

Figure 3.2: Generated distribution of the nodes in two cross-sections through the cylindrical tank in two planes $z = H/2$ and $\phi = 0$

Depending on the necessary accuracy to resolve given phenomena we applied multiple refinements on the basic grid (figure 3.2) used. Considered basic grid consisting of 140 elements, which were distributed based on the level of interest for resolving specified regions (eg. boundary layers). Mentioned distribution can be recognized close to the boundaries and axial region in figure 3.2 A notable perk of Nek5000 is its capability of dealing with elements, which boundaries consist of straight as well as curved walls. We use this feature to discretize the domain into different shaped elements. Therefore, the domain is radially speaking most accurately refined near the boundaries $r = [0.95, 1]$, where two curved sided elements are applied. Moving towards the axis, in the region of the core flow $r = [0.45, 0.9]$ the size of the elements is increased and the walls of the elements are straight and less refined. Conclusively the axial area $r = [0, 0.45]$ is again refined and consists of straight sided elements. To decrease the roughness of transition between curved and straight sided element, we introduce transitional regions, which we refine additionally. The refined areas near angles with multiples of $\frac{\pi}{4}$ are residuals of the grid generation. Wherein a sections of $\frac{\pi}{4}$ is created, duplicated and rotated. To smooth the transition between those sections, these refined areas are introduced.

During the computations described in Chapter 4 multiple grades of overall refined grids were

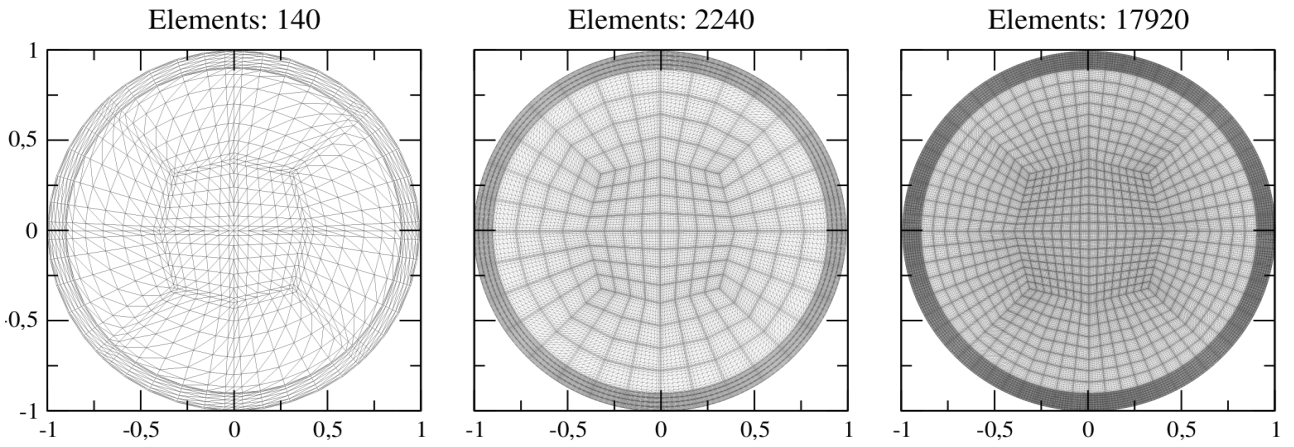

Figure 3.3: Applied refined grids, starting from 140 elements ($left$) to a intermediate grid of 2240 elements ($middle$) and a grid of 17920 elements ($right$)

required leading to a maximum amount of 17920 elements. Figure 3.3 shows the progress of refinement over the different grids.

3.3 Streamline

We compute the streamline topology of the three-dimensional flow and its properties within a Lagrangian representation of the fluid kinematics. Therefore, we introduce $\boldsymbol{X}$ denoting the position of an infinitesimal fluid element. Setting the initial condition to $\boldsymbol{X}_0 = \boldsymbol{X}(t = 0)$, its motion is governed by

$$\frac{d\boldsymbol{X}}{dt} = \boldsymbol{u}(\boldsymbol{X}). \tag{3.19}$$

The computing algorithm applied is a MATLAB based code using a linear interpolation scheme to reconstruct the velocity field. Furthermore, we integrate the incompressible Euler equations applying the Runge Kutta 4(5) Dormand-Prince method to compute the streamlines starting from various initial points. To avoid any loss of accuracy by switching to a linear interpolation method, we increased the number of elements by a factor of 128. Therefore, the applied grid was generated using a quadratic refinement method within two refinement steps and interpolated spectrally on the new grid. Leading to a grid size consisting out of 17920 elements,

previously shown in figure 3.3 (right). The applied code uses the within MATLAB implemented **ode45** solver, which is an ordinary differential equation solver, using the Dormand and Prince algorithm [17]. The Dormand and Prince algorithm is a highly accurate, six-stage, fifth-order Runge-Kutta based method. With an error esitmate of always less than 10^{-7}

Chapter 4

Results

4.1 Flow

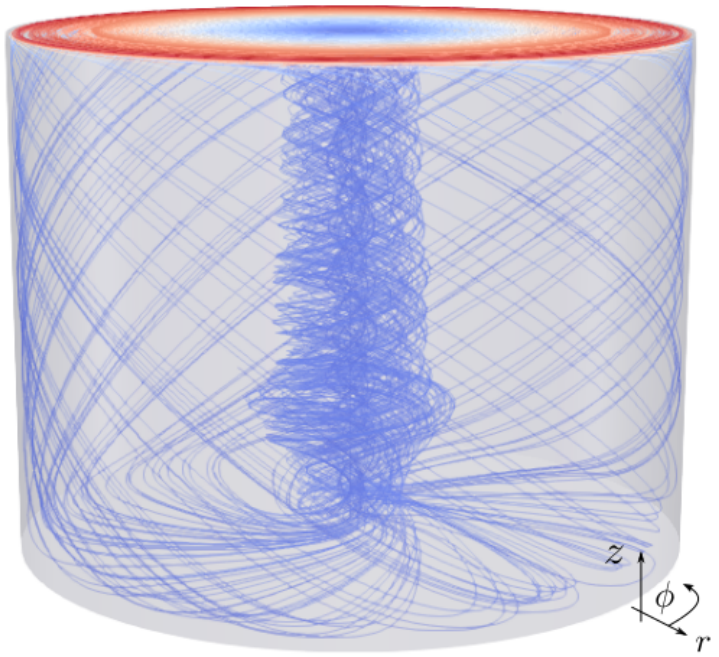

Figure 4.1: A qualitative depiction of the streamline topology of the flow obtained for $\gamma = 2.0$ and $Re = 1800$. Red colored streamlines represent fluid elements of high velocity, whereas blue characterizes low velocity.

volume forces

Driven by the angular velocity of the rotating top endwall, the velocity of the axially drawn

fluid increases towards the top upper boundary, where it is ejected in a spiraling motion along the cylindrical wall. When reaching the bottom endwall, the downward forced spiral is forced towards the axis of the fixed endwall and then again turns into the axial direction towards the rotating upper endwall. The inward spiraling motion results in an initial increase in swirl velocity, due to conservation of angular momentum, and so the creation of a concentrated vortex. Computations are continued till the solution converges to a steady result for axisymmetric cases and stationarity in the rotating frame of reference for travelling waves. Fig. 4.1 represents an overview of the observed flow for $\gamma = 2$ and $Re = 1800$.

4.2 Vortex Breakdown

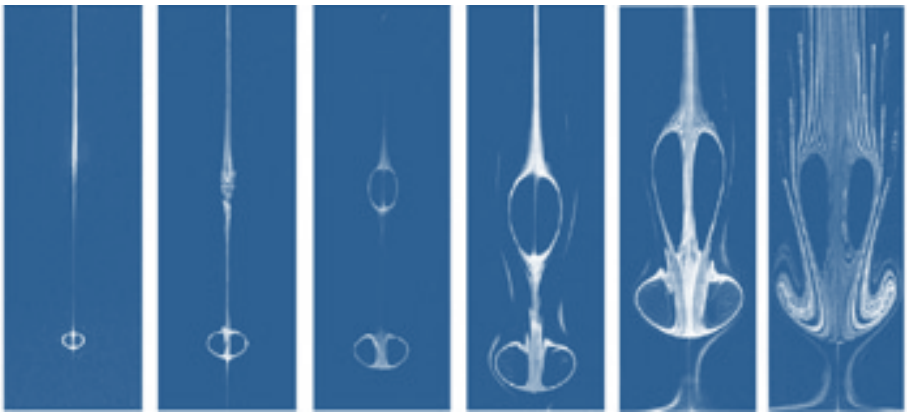

Figure 4.2: Experimental visualization of the changes in the vortex structure with increasing Re by Escudier [5]. Shown visualization represents $\gamma = 2.5$ for a range in $Re = 1918, 1942, 1994, 2126, 2494, 2765$ from left to right. Due to opposite driving lids the original plots are mirrored with respect to $z = \gamma/2$ for consistency with the position of the driving lid in our simulations (top).

By injecting dye axially through a hole within the steady lid into the experimental setup it has been shown [5], that for Reynolds numbers above a certain threshold a phenomenon along the axis of rotation - further on called *vortex breakdown* - can be observed (Fig. 4.2). For certain combinations of Re and γ up to three vortex breakdowns along the axis may occur. Varying these two parameters Escudier obtained a map of the regions of appearance for those vortex breakdowns. Furthermore it has been shown that the stationarity of the overall system is based on those two parameters and is only given in a restricted region. Results of investigations by

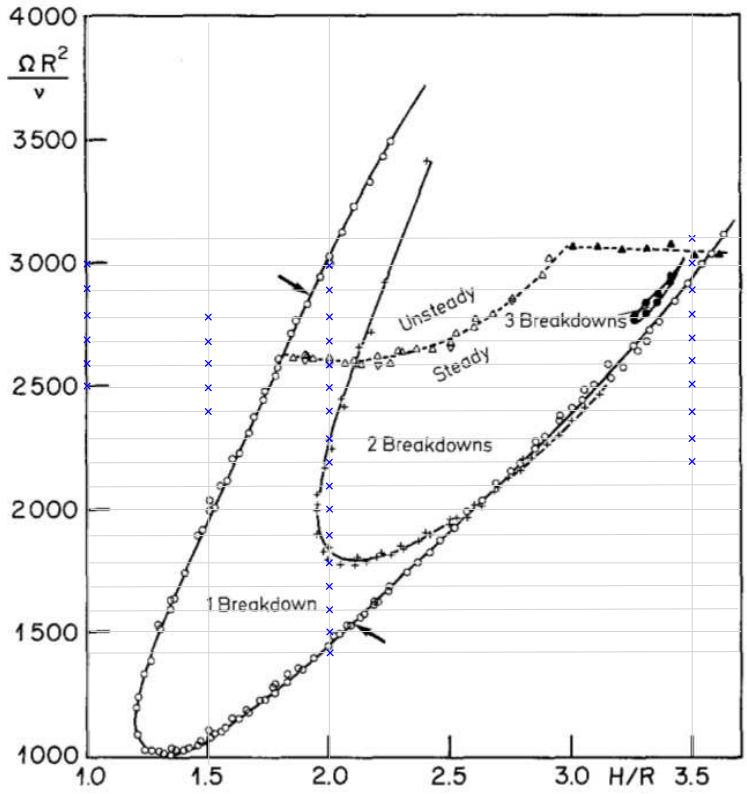

Figure 4.3: Quantitative representation of the experimental results by Escudier [5]. Blue crosses represent parameter value combinations corresponding to simulations conducted in the frame of this thesis.

Escudier are summarized in the plot represented by Fig. 4.3. Blue crosses mark simulations done in the frame of this thesis, which are additionally summarized in table 4.1.

		Re																	
		1400	1500	1600	1700	1800	1900	2000	2100	2200	2300	2400	2500	2600	2700	2800	2900	3000	3100
γ	1.0												x	x	x	x	x	x	
	1.5											x	x	x	x	x			
	2.0	x	x	x	x	x	x	x	x	x	x	x	x	x	x	x	x	x	
	3.5									x	x	x	x	x	x	x	x	x	x

Table 4.1: Summarization of parameter value combinations covered by simulations.

Beside a quantitative validation of our carried out simulations with NEK5000 via a comparison of the topology of the flow found by Escudier with resulting visualizations of simulations, a quantitative comparison with experimental measurements is approached.

The comparison of experimental and numerical results is done by investigating the axial velocity w along the axis of rotation of the cylinder. By choosing $\gamma = 2.0$ we cover multiple states

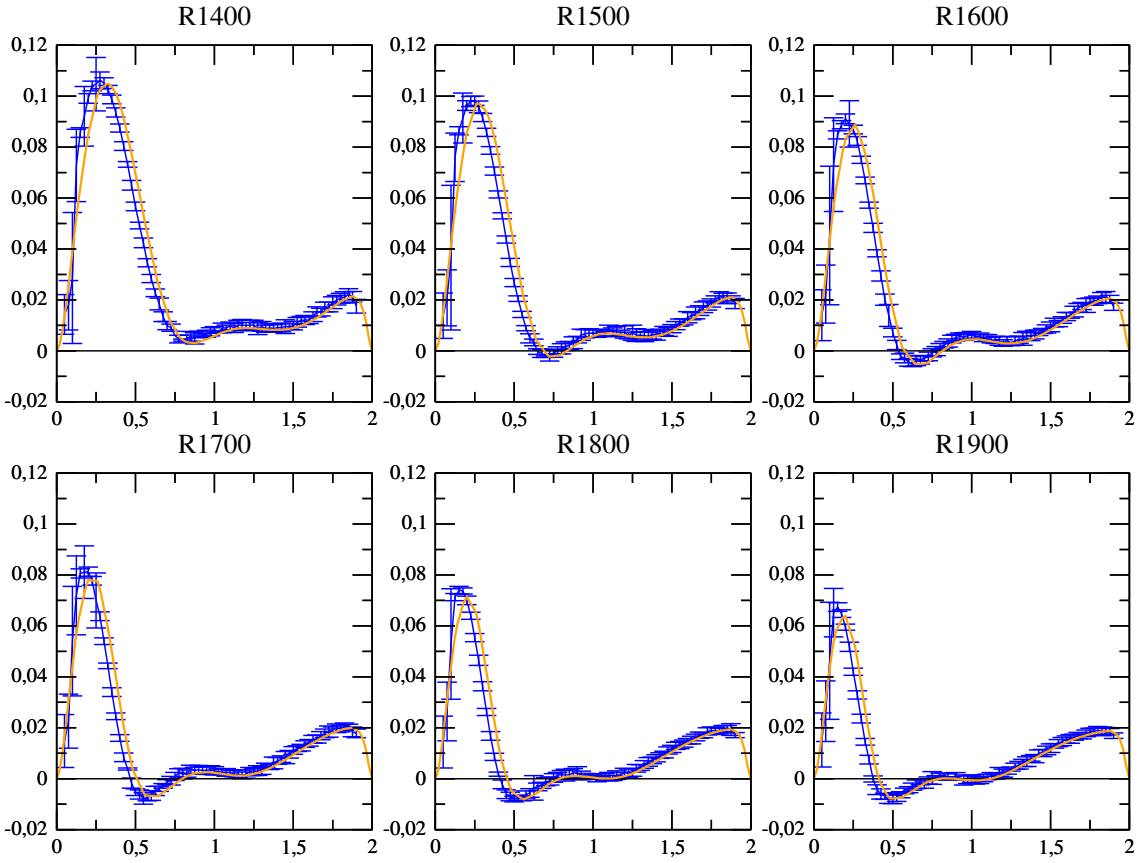

Figure 4.4: Comparison of numerical results (orange) to experimental measurements (blue) for $\gamma = 2.0$ in a range of $Re = [1400, 1900]$. Experimental data courtesy of H. Wu.

of the system by varying Re, ranging from a non existence of the vortex breakdown up to the regime where 2 breakdowns occur. The points of interest for this variation are set in range between $Re = [1400, 2500]$ for a step-size of $\Delta Re = 100$, excluding areas of unsteady motion (see Fig. 4.3). Figure 4.4 shows this comparison for a range of Reynolds Numbers in $[1400, 1900]$. The blue line represents the experimental data including error bars for the experimental measurements, whereas the orange line refers to data acquired from the numerical simulations. One can see an overall match between numerical and experimental results within given error bars for experimental data. Furthermore one should emphasize in particular values of $w = 0$ appearing in pairs, which are indicating stagnation points of the flow along the axis of rotation. They are representative for the axial length of a vortex breakdown for observed Reynolds number, which initially occurrence is shown for $\gamma = 2.0$ at $Re = 1500$ located between $z = [0.6, 0.8]$ (see Fig. 4.4 and 4.3). For a parameter combination of $\gamma = 2.0$ and $Re = 1900$ one can observe the entity of another vortex breakdown between $z = [0.7, 1.2]$.

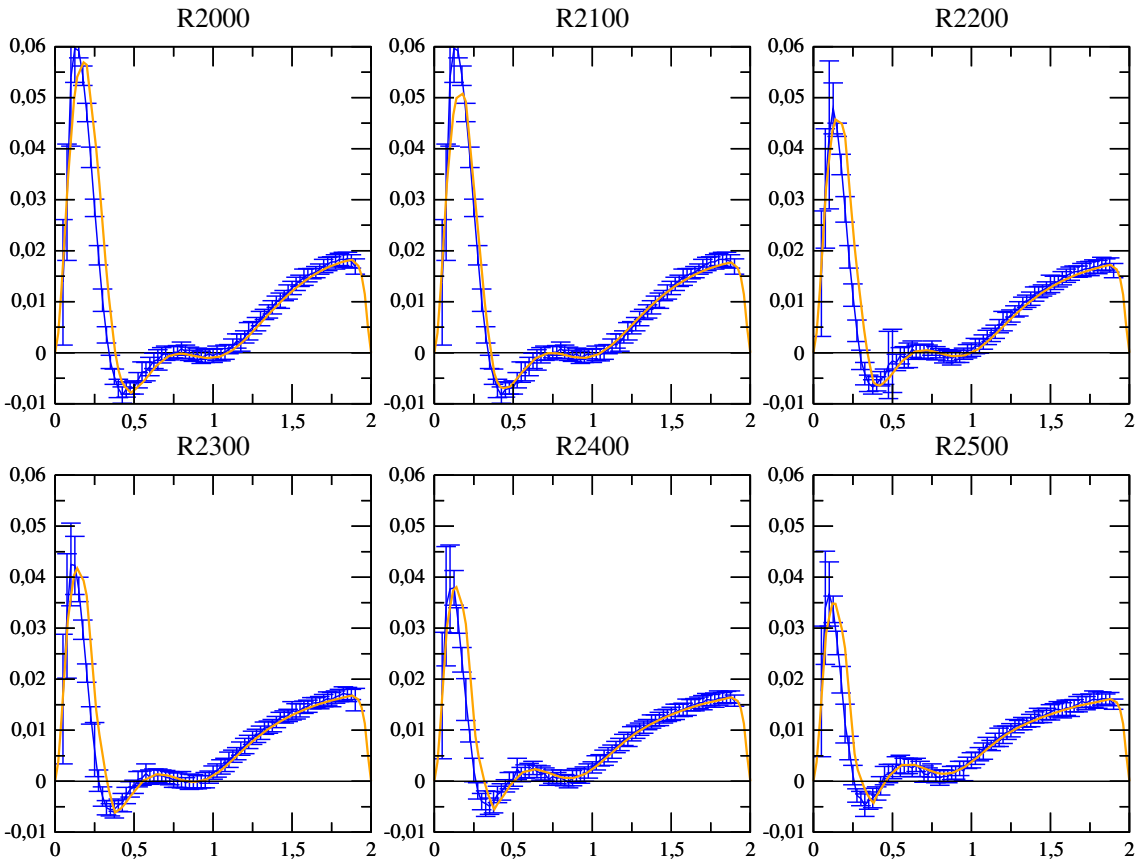

Figure 4.5: Comparison of numerical results (orange) to experimental measurements (blue) for $\gamma = 2.0$ in a range of $Re = [2000, 2500]$. Experimental data courtesy of H. Wu.

An overall trend in reducing w along the axis with increasing Re is recognizable. The reduction is remarkably visible at distances close to the bottom lid $z = [0, 0.75]$. This is a result from the scaling itself, which is independent on the change of the rescaled flow. The change of the rescaled flow is dependent on the Reynolds number. Fig. 4.4 shows that increasing Re reduces the w velocity component close to the axis at the top lid.

For cases in the range of $Re = [2000, 2500]$ we enter at $Re = 1900$ and exit at $Re = 2300$ the 2-breakdown regime (compare Fig. 4.5 and Fig. 4.3). The overall trend of a decreasing axial velocity w is continued, decreasing the maximum w from $w(Re = 1400) = 0.15$ to $w(Re = 2500) = 0.035$ (almost a factor 5). One observes the overall agreement for numerical results with experimental measurements, except for the case $Re = 2100$, where locally numerical and experimental data do not overlap. Further results for simulations for $Re > 2500$ are in agreement with the experimentally observed unsteady behavior, wherein the vortex breakdown vertically oscillates along the centerline of the cylindrical container.

Summarizing made observations one can deduce the following: An increase in Reynolds number leads to an reduction of the boundary layer thickness at the rotating endwall. The boundary layer sustains the circulating motion. Therefore, decreasing its thickness reduces the axial component of the velocity in the inner core of the flow.

4.3 Traveling Waves

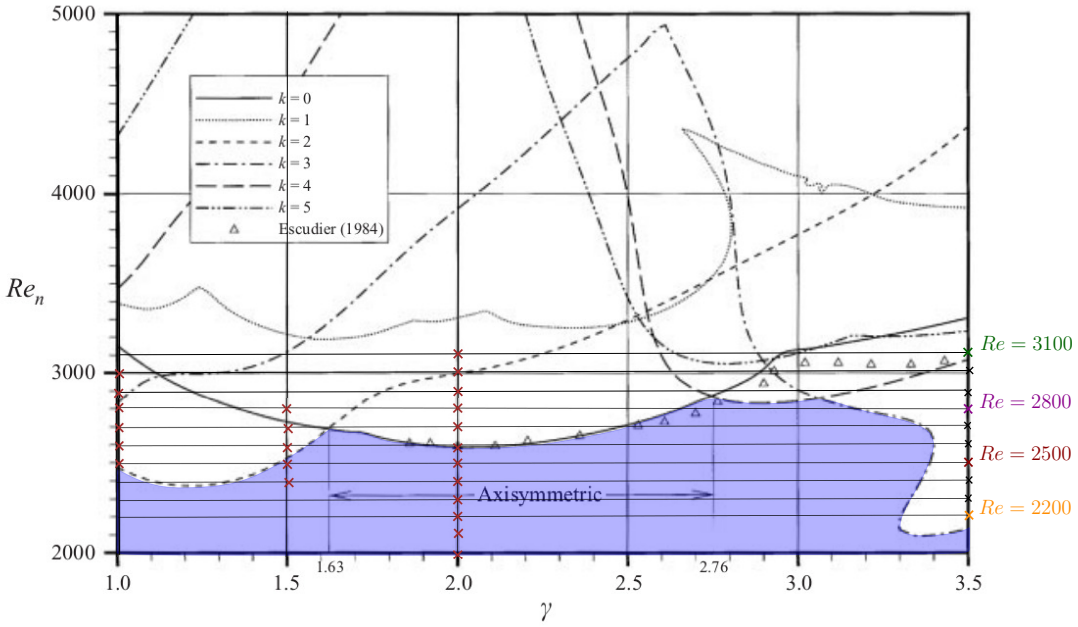

Figure 4.6: Neutral Reynolds numbers $Re_n(\gamma, k)$ and critical Reynolds numbers $Re_{cr}(\gamma, k)$ over γ. Brown crosses represent simulation conducted in the frame of this thesis. Blue colored area depicts the threshold underneath $Re_{cr}(\gamma, k)$, wherein no traveling waves occur. Plot by Gelfgat et al. [6].

Beside the previously described topological phenomenon, the existence of traveling waves with modes k has been shown by Gelfgat et al. [6] in a lid driven cylindrical container. The modes k vary within the investigated parameter space in a range of $k = [0, 5]$, whereas $k = 0$ corresponds to an azimuthal perturbation. Figure 4.6 depicts the results drawn from linear stability analysis for the critical wavenumber k_{cr}. The integer value k_{cr} at a critical Re_{cr} correspond to a threshold, which is called neutral stability curve. This threshold denotes the minimum values in Re, which denotes the onset of an instability. In Fig. 4.6 $Re_{cr}(\gamma)$ corresponds to a line separating the parameter space. $Re < Re_{cr}(\gamma)$ corresponds to the blue colored area in which instabilities are non-existent. Probing the flow at $\boldsymbol{x} = (x, y, z) = [0.6175, 0.3090, 2.0086]$ for $\gamma = 3.5$ reveals the occurrence of traveling waves after dependencies due to initial conditions vanish (Fig. 4.7).

Considering traveling waves as a perturbation with respect to the mean-flow. One can write in general:

$$\boldsymbol{u} = \bar{\boldsymbol{u}} + \boldsymbol{u'} \tag{4.1}$$

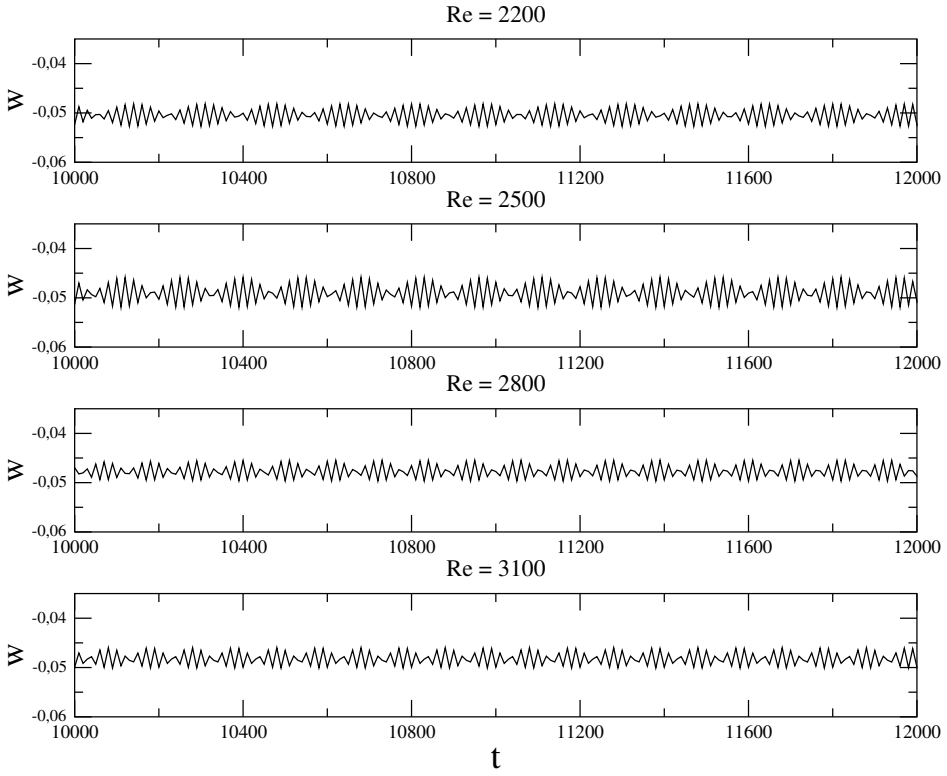

Figure 4.7: Occurrence of a traveling wave for $\gamma = 3.5$ for $Re = 2200, 2500, 2800, 3100$. The axial velocity w over time t probed at $(x, y, z) = (0.6175, 0.3090, 2.0086)$.

Wherein $\bar{\boldsymbol{u}}$ denotes the mean-flow velocity and $\boldsymbol{u'}$ deviations from such, which we refer to as perturbations. By computing the perturbation by $\boldsymbol{u'} = \boldsymbol{u} - \bar{\boldsymbol{u}}$, one can detect and visualize their time dependency. For parameters $\gamma = 1.5$ and $Re = 2600$ one can observe a traveling wave with $k = 2$, which is shown in figure 4.8. The components of $\boldsymbol{u}$ are given in a cylindrical coordinate system as $\boldsymbol{u} = f(u_r, u_\phi, u_z)$. Similar patterns were published by Gelfgat et al [6]. By measuring the value of the axial component of $\boldsymbol{u}$ in a given point $\boldsymbol{x} = (x, y, z) = [0.6175, 0.3090, 2.0086]$ over time, one can determine the frequency f of such a traveling wave and further its angular velocity ω. Emphasizing a stable steady motion it can be concluded given the measured frequency f_m, that for $k > 0$ the frequency f is determined by $f = \frac{f_m}{k}$.

By applying this procedure for different Reynolds numbers within an aspect ratio near to Re_{cr}, one converges towards the critical Reynolds number Re_{cr}. Whereas flow-fields for $Re < Re_{cr}$ does not include traveling waves. Results have been shown by Gelfgat et al within Figure 4.9, including experimental data for $1.87 \leq \gamma \leq 3.5$. Validating the code in use, an agreement

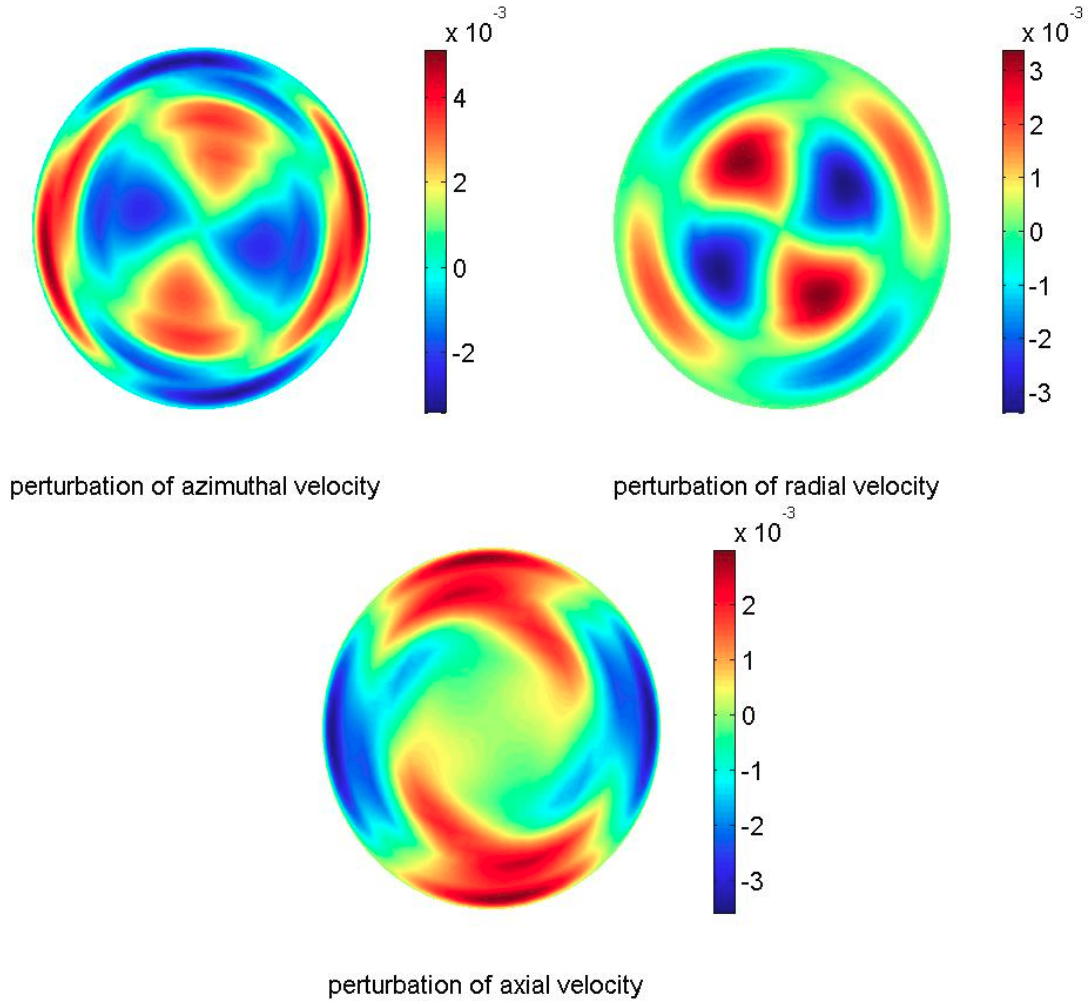

Figure 4.8: Cross-section at $z = 1.0$ showing a traveling wave with mode $k = 2$ for $\gamma = 2.0$, $Re = 2600$. Visualized as $\boldsymbol{u'} = \bar{\boldsymbol{u}} - \boldsymbol{u}$ for cylindrical velocity components.

within corresponding has been shown for $\gamma = [1.5, 3.5]$.

		Re					
		2200	2500	2600	2650	2800	3100
γ	1.5		0.0113	0.0354			
	3.5	-0.2785	-0.3021			-0.3964	-0.4214

Table 4.2: Summarization of evaluated neutral frequencies.

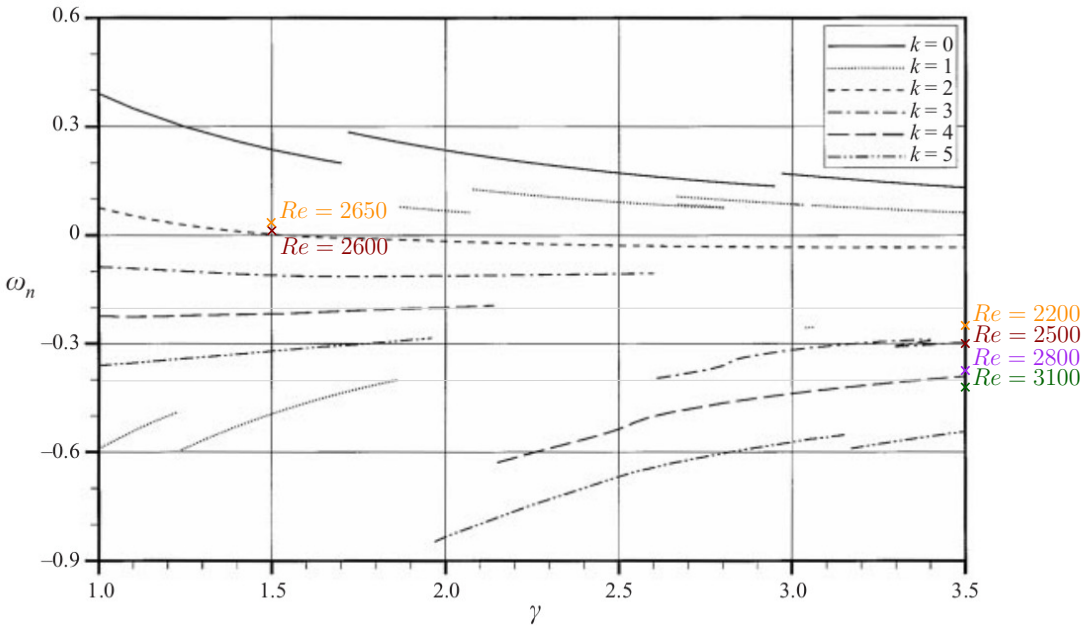

Figure 4.9: Dependency of the neutral frequency $\omega_n(\gamma, k)$ on the aspect ratio γ and number of modes k. Colored crosses represent computed ω_n for depicted Re. Plot by Gelfgat et al. 4.9.

Showing this additional instability phenomenon provides a further validation of the code. The appearance of instabilities in a lid driven cylinder is limited to an area above the neutral stability curve. Values for this threshold are depending on the aspect ratio, shown within figure 4.6 by Gelfgat et al including experimental data by Escudier. For $\gamma = 1.5, 2.0, 3.5$ it can be observed that obtained neutral stability values were in agreement with numerical results. A summarization of evaluated ω_n is given in tab. 4.2, which are additionally implemented in fig. 4.9.

4.4 Streamline Topology

Considering $\gamma = 3.5$ we study the dependency of the flow topology in a reference frame rotating with the angular velocity of the travelling wave, i.e. $\boldsymbol{u} - \Omega r \boldsymbol{e}_\phi$ using Poincarè sections in a half-plane for $\phi = 0$ for $Re = 2200, 2500, 2800, 3100$. The phase of the travelling wave is fixed taking a snapshot of the flow at $t = 12000$ (see fig. 4.7) One can observe the development of up to three vortex breakdowns for $Re = 3100$. Starting at $Re = 2200$ close to the axial region around $\boldsymbol{x}(r, \phi, z) = \boldsymbol{x}(0, 0, 3)$ the flow-field is deformed and one can find the first breakdown bubble

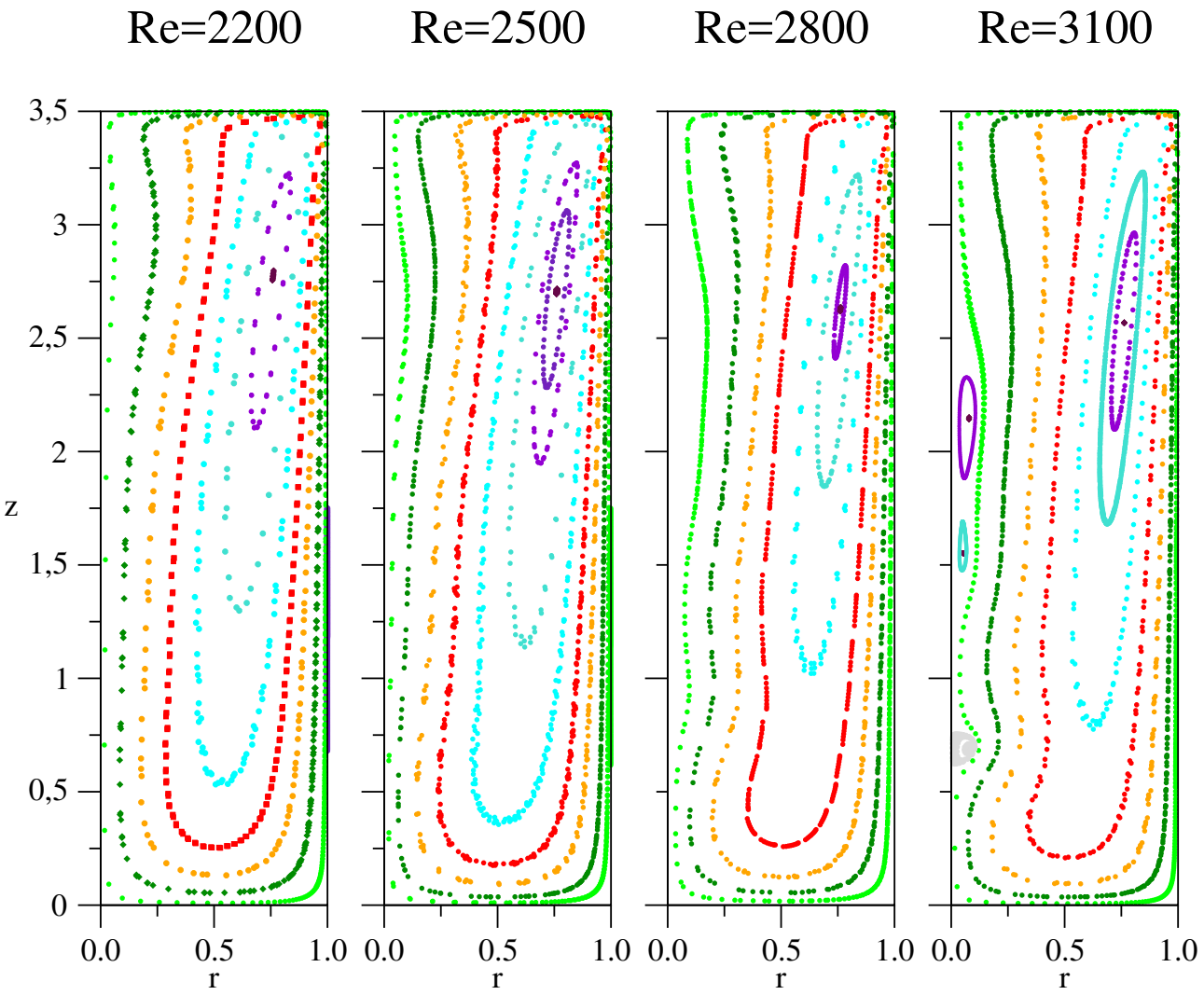

Figure 4.10: Poincarè sections for $\gamma = 3.5$ for $Re = 2200, 2500, 2800, 3100$. Sections are rotated at a frequency f dependent on Re. Given frequencies were $f_{2200} = 0.40$, $f_{2500} = 0.44$, $f_{2800} = 0.61$ and $f_{3100} = 1.50$ Dots denote the point of intersection of streamlines through the plane. Colors identify of the streamline. Black dots show the elliptic points which belong to the periodic streamlines.

occurring at $Re = 2500$ (not shown). Observed vortex breakdown enlarges at $Re = 2800$ (not shown). For $Re = 3200$ the vortex breakdown splits into two separated closed bubbles and forms an additional bubble close to the bottom wall. Figure 4.10 summarizes Poincarè sections produced for $\gamma = 3.5$ and $Re = 2200, 2500, 2800, 3100$. One finds an overall regular regions of flow attracting close by streamlines, which admits a toroidal topology. These tori are known as KAM tori. Named after Kolmogorov, Arnold and Moser, who derived the relevant theorem stating conditions under which chaos is restricted in extent. For further information about the theory behind chaotic advection the reader is referred to H. Aref [18]. The coordinates of the periodic streamline together with the dependency with respect to Re are summarized in table 4.3, showing the tendency of shifting towards the bottom wall for higher Re.

		Re			
		2200	2500	2800	3100
$\gamma = 3.5$	r	0.756	0.780	0.775	0.756
	z	2.786	2.694	2.608	2.559

Table 4.3: Coordinates of the periodic streamline in figure 4.10.

We observe for $\gamma = 3.5$ and $Re = 3100$ a chaotic region (see grey colored markers in fig. 4.10) which invaded the structurally unstable recirculation bubble, as it was predicted by Sotiropoulos et al. [19].

Given these observation we concern the stability of the basic flow. One could conclude two possibilities. Firstly the main rotating flow serves as a highly dominant regularizing mechanism. This motion dominates the dynamics of the flow and does not allow for the onset of chaotic motion. Or secondly, the idealized approach of numerical simulations suppresses imperfections of the real system, which would lead to the onset chaotic motions in an experiment.

4.4.1 Perturbed Flow

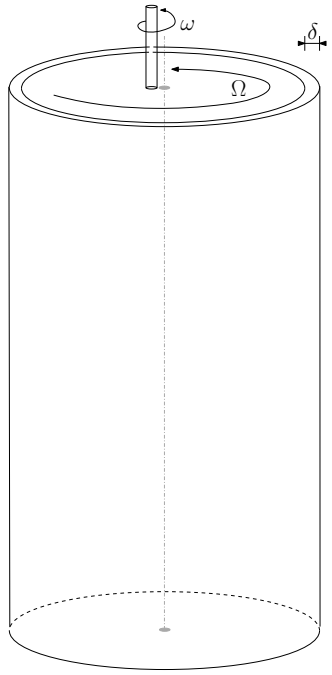

Figure 4.11: Sketch showing the applied perturbation for $\gamma = 3.5$

We want to rule out the second possibility by adding an artificial imperfection to the numerical simulation, which shall mimic the most likely imperfection in an experimental setup, which we consider to be a misalignment of the shaft with the axis of the cylinder with a small gap δ at the interface of the top lid and the side wall. The misalignment results in an additional rotation of the shaft around the axis of the cylinder (see fig. 4.11. To realize such, an artificial flow-field has been simulated, which is considered as artificial perturbation and superposed on the existing flow-field for $\gamma = 3.5$ and $Re = 3200$. An additional perturbation flow is computed solving the Stokesian flow with the following boundary conditions at the moving lid.

$$u_x = -\frac{y/\left[0.005(\pi/2+1)\right]\ \ (atan(0.95-\sqrt{x_{mD}^2+y^2})}{2\ a_z} \tag{4.2}$$

$$u_y = \frac{y/\left[0.005(\pi/2+1)\right]\ \ (atan(0.95-\sqrt{x_{mD}^2+y^2})}{2\ a_z} \tag{4.3}$$

Wherein $x_{mD} = (x - 0.05)$, $a_z = [(z - z_{\text{start}})/(3.5 - z_{\text{start}})]^5$ and z_{start} is set to 0. Again using Poincarè sections, figure 4.12 summarizes the results of this numerical experiment. Clearly showing the regularity of the streamlines is not very influenced amplifying the perturbation. The effect can be weakly recognized in the axial region near the upper lid $\boldsymbol{x}(r, \phi, z) = \boldsymbol{x}(0, 0, 3.4)$, where the scale in magnitude of perturbation to general flow-field is more significant than in other regions.

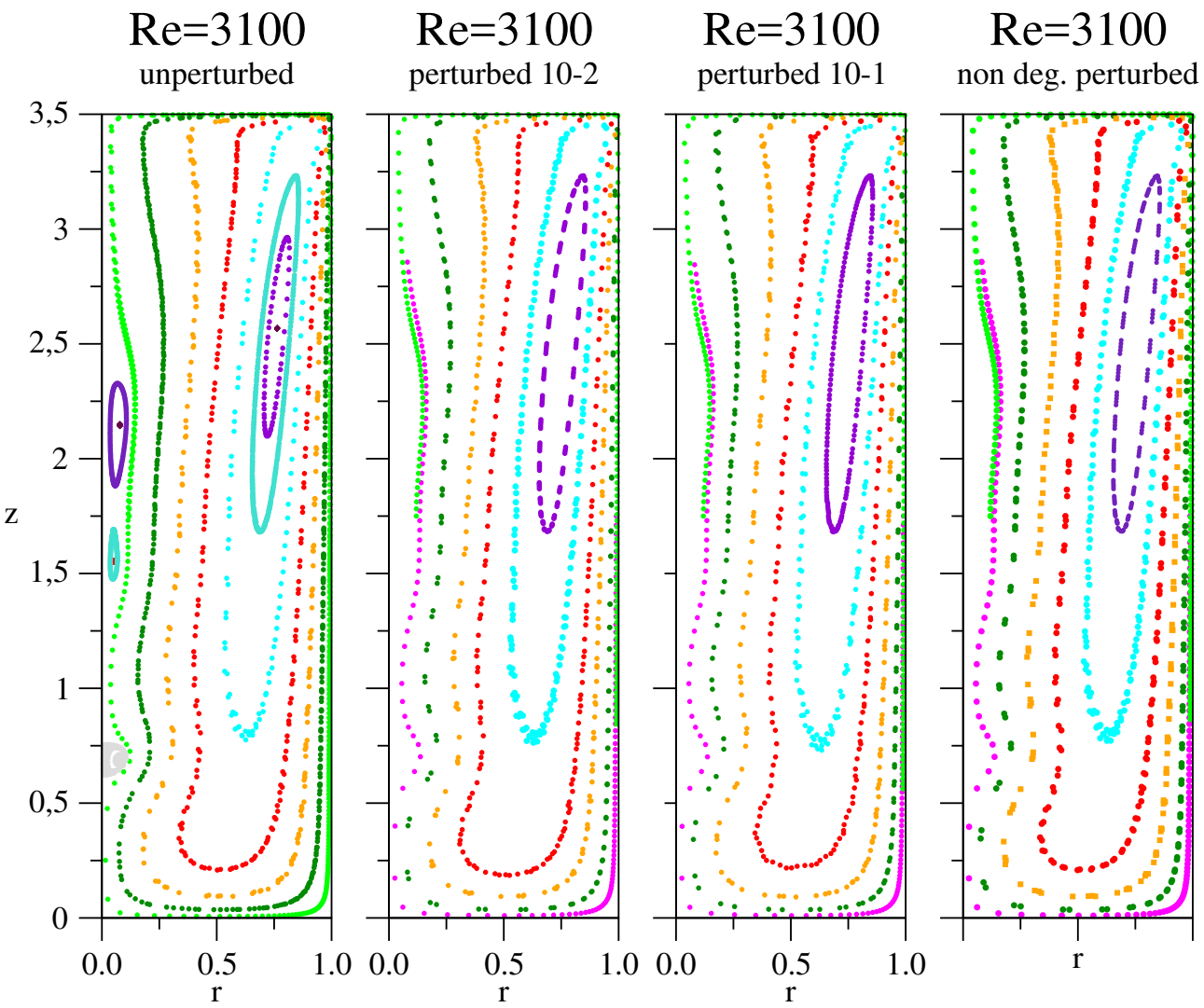

Figure 4.12: Poincarè sections for $\gamma = 3.5$ for $Re = 3100$. Dots denote the point of trespass of a streamline through the plane. Colors indicate the identity of the streamline. Black dots show the periodic streamlines.

Increasing the perturbation in magnitude further can not be considered as slight imperfections of the system, which would lead to unphysical results by pushing this numerical investigation furthermore.

The additional perturbation is formulated as:

$$u_r = -A\ R(1-R)\ \frac{\pi}{\gamma}\ \left(\frac{\pi z}{\gamma}\right) \tag{4.4}$$

$$u_z = -A\ R(3R-2)\ sin\left(\frac{\pi z}{\gamma}\right) \tag{4.5}$$

Setting $\Gamma = 1$, A is used as a scaling factor for the size of the perturbation, chosen within a range of 10^{-2},10^{-1} and a case with a non degenerating connection between the saddle foci s1 and s2 located along the axis over the two cylinder's bases. This means that the no-slip condition all over the cylinder walls is eliminated by the perturbation (4.4) and (4.4.1) superposed to the Navier-Stokes solution. The reasoning behind this implementation was to create conditions of a non degenerate perturbation. However, including this possibility does not lead to any significant differences in the topology.

Based on this observation we consider that the rotating motion has a dominant regularizing mechanism on the streamlines, which dominates over the flow perturbations.

Chapter 5

Conclusion

In the frame of this work, we have numerically studied multiple appearing flow structures in the setup of a lid driven cylinder, reaching from vortex breakdowns, over traveling waves, to KAM tori. Due to our demand for accuracy and efficiency we applied the spectral element solver NEK5000 for solving Navier-Stokes equations. The applied code was verified by comparing our results with literature as well as experimental measurements. For this verification we mainly focused on the work of Escudier [2] and Gelfgat et al. [6], for both references we showed an agreement with our computational results. The core frame of this thesis was aimed towards the understanding of the occurring KAM tori and on the proof of coexistent regular and chaotic regions of the flow, in a Lagrangian topological sense. Our investigations did not provided evidence which support the second claim. However, we showed the robustness of regularity within the proposed configurations for a range of artificial perturbations. Furthermore, we speculate the swirling motion has a dominant regularizing effect on the flow streamlines, even when additional perturbations are superposed.

Summarizing, the rotational driving force shapes the topology of the flow field into a spiralling motion arranged by 2 co-rotating spiralling saddle foci. A spiral motion drives the flow near the stationary cylindrical walls, which incorporates an upward facing spiral at the axis of rotation. Observations made in chapter 4 let us conclude, that one can distinguish this overall motion furthermore. Therefore, we decompose the overall flow based on the shape of the local

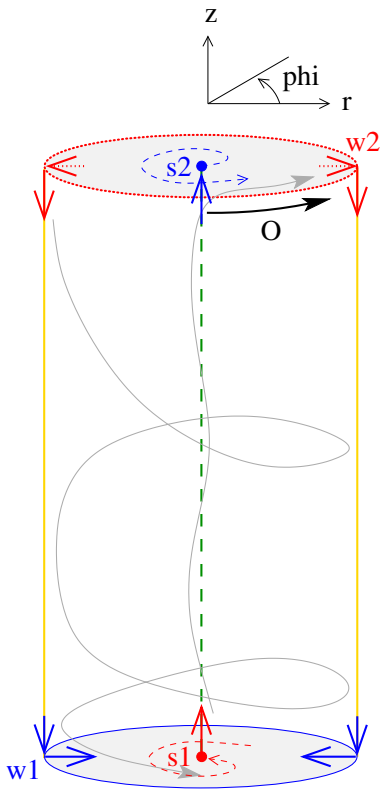

Figure 5.1: A schematic sketch of the streamline of near wall and near axis streamlines. The setup is decomposed into four regions due to different behavior in motion. (1) The top lid (*red*) forcing the flow in an outward spiral away from the saddle focus ($s2$) to the top circular edge ($w2$). (2) The streamlines at the cylindrical wall (*yellow*) changing the direction of motion to a downward facing spiral ending at the bottom circular edge ($w1$). (3) Reaching the bottom lid (*blue*) the direction of the streamlines changes to an inward facing spiral with a saddle focus ($s1$) at its center. (4) Streamlines along the axis connect both saddle foci with an upward spiral.

streamlines, which one can deduce based on the Poincarè sections computed in section 4.4. The rotating top lid generates a distributing, outward facing spiralling motion from the axial saddle focus $s2$, which intakes fluid axially. The axial flow itself connects this distributing motion at the top lid with the collecting motion at the bottom lid, where an inward facing spiral with a saddle focus $s1$ at the axis of the cylinder collects fluid from the cylindrical walls and ejects it axially, feeding the axial motion, which is connecting $s1$ with $s2$. The streamlines near the cylindrical walls describe a heteroclinic connection, connecting $s2$ with $s1$ through two degenerating limit cycles $w1$ and $w2$. Figure 5.1 illustrates these observations schematically, based on the streamlines of near wall and near axis fluid. Figure 5.2 summarizes made observations concerning distributing and collecting motion. The streamline topology indicates a heteroclinic connection.

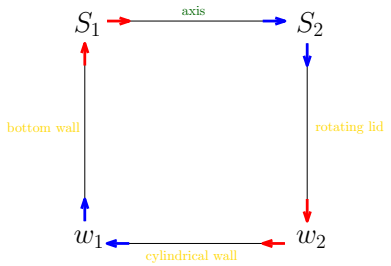

Figure 5.2: Schematic summarizations of distribution and collecting mechanism within the lid driven cylinder setup.

However, the possibility of the origin of chaotic dynamics in a lid driven cylindrical tank has been identified for the three-dimensional stationary vortex-breakdown bubble for an aspect ratio of $H/R = 1.75$ [19] . Sotiropoulos et al. show that the onset of chaotic motion is connected with the appearance of Shilnikov orbits. Therefore, the motion within the lid driven cylindrical tank allows in general the onset of chaotic motion, but not for the here observed degenerate connection $w1 \to s1 \to s2 \to w2 \to w1$.

Future work concerning the lid driven cylindrical container should aim for further investigations towards the stability of the flow. While Shilnikov orbits signal the onset of chaotic dynamics [20], it has been speculated that the swirling flow regularizes the topology of the main flow. Remaining questions lie within the understanding of the limits of this mechanism and concern how the transition to chaos occurs. Therefore, future investigations should be considered for an aspect ratio for which both saddle foci are sufficiently close.

Bibliography

[1] M. Sharif, "Laminar mixed convection in shallow inclined driven cavities with hot moving lid on top and cooled from bottom," *Appl. Therm. Eng.*, vol. 27, no. 5, pp. 1036 – 1042, 2007.

[2] M. Escudier, "Confined vortices in flow machinery," *Annu. Rev. Fluid Mech.*, vol. 19, no. 1, pp. 27–52, 1987.

[3] K. Khanafer and S. Aithal, "Laminar mixed convection flow and heat transfer characteristics in a lid driven cavity with a circular cylinder," *Int. J. Heat Mass Transf.*, vol. 66, no. Supplement C, pp. 200 – 209, 2013.

[4] H. Vogel, *Experimentelle Ergebnisse über die laminare Strömung in einem zylindrischen Gehäuse mit darin rotierender Scheibe*. Max-Planck-Institut für Strömungsforschung, MPI Strömungsforschung, 1968.

[5] M. P. Escudier, "Observations of the flow produced in a cylindrical container by a rotating endwall," *Exp. Fluids*, vol. 2, no. 4, pp. 189–196, 1984.

[6] A. Y. Geflgat, P. Z. Bar-Yospeh, and A. Solan, "Three-dimensional instability of axisymmetric flow in a rotating lidcylinder enclosure," *J. Fluid Mech.*, vol. 438, p. 363377, 2001.

[7] J. N. Sørensen, I. Naumov, and R. Mikkelsen, "Experiments on three-dimensional instabilities in a confined flow generated by a rotating lid," *J. Phys. Conf. Ser.*, vol. 64, no. 1, p. 012013, 2007.

[8] T. V. Kármán, "Über laminare und turbulente Reibung," *J. Appl. Math. Mech.*, vol. 1, no. 4, pp. 233–252, 1921.

[9] O. Reynolds, "An experimental investigation of the circumstances which determine whether the motion of water shall be direct or sinuous, and of the law of resistance in parallel channels," *Philos. Trans. Royal Soc.*, vol. 174, pp. 935–982, 1883.

[10] A. T. Patera, "A spectral element method for fluid dynamics: Laminar flow in a channel expansion," *J. Comput. Phys.*, vol. 54, no. 3, pp. 468 – 488, 1984.

[11] J. W. L. Paul F. Fischer and S. G. Kerkemeier, "nek5000 Web page," 2008. http://nek5000.mcs.anl.gov.

[12] M. O. Deville, P. F. Fischer, and E. H. Mund, *High-Order Methods for Incompressible Fluid Flow*. Cambridge Monographs on Applied and Computational Mathematics, Cambridge University Press, 2002.

[13] J.-C. Loiseau, *Dynamics and global stability analysis of three-dimensional flows*. Thesis, Ecole nationale supérieure d'arts et métiers - ENSAM, 2014.

[14] A. Quarteroni, *Numerical Models for Differential Problmes*. Springer Nature, 2017.

[15] P. A. T. Maday, Y. and E. M. Rønquist, "An operator-integration-factor splitting method for time-dependent problems: Application to incompressible fluid flow," *SIAM J. Sci. Comput.*, vol. 5, no. 4, pp. 263–292, 1990.

[16] H. Uzawa and K. J. Arrow, *Iterative methods for concave programming*, p. 135148. Cambridge University Press, 1989.

[17] J. Dormand and P. Prince, "A family of embedded Runge-Kutta formulae," *J. Comput. Appl. Math.*, vol. 6, no. 1, pp. 19 – 26, 1980.

[18] A. H., "The development of chaotic advection," *Phys. Fluids*, vol. 14, no. 4, pp. 1315–1325, 2002.

[19] F. Sotiropoulos, Y. Vonetikos, and T. C. Lackey, "Chaotic advection in three-dimensional stationary vortex-breakdown bubbles: Shil'nikov's chaos and the devil's staircase," *J. Fluid Mech.*, vol. 444, p. 257297, 2001.

[20] V. S. Afraimovich, S. V. Gonchenko, L. M. Lerman, A. L. Shilnikov, and D. V. Turaev, "Scientific heritage of L.P. Shilnikov," *Regul. Chaotic Dyn.*, vol. 19, no. 4, pp. 435–460, 2014.